引用格式：WANG Kehong, YU Yang, WANG Yang, et al. Comparative Study on Temperature Sensing Characteristics of Dual Mechanisms in Hollow Core Fiber[J]. Acta Photonica Sinica, 2022, 51(11):1106001
汪柯红,余洋,王洋,等.空芯光纤的双机理温度传感特性比较[J].光子学报,2022,51(11):1106001

空芯光纤的双机理温度传感特性比较

汪柯红,余洋,王洋,刘笑尘,赵帅昌,杨勇,张琦,张小贝
(上海大学 通信与信息工程学院,特种光纤与光接入网重点实验室,上海 200444)

摘　要:实现了一种基于负曲率反谐振空芯光纤的级联型光纤传感器件,并从理论和实验上分别研究了其反谐振干涉和多模干涉两种机理的温度传感特性。器件由单模光纤、渐变折射率多模光纤与空芯光纤级联熔接制成,在实现高效率耦合下,基于两种机理实现温度传感并进行比较研究。仿真分析了空芯光纤的纤芯模式和包层管模式,基于光纤材料的热膨胀和热光效应理论研究了温度传感特性。实验结果表明,基于反谐振干涉和多模干涉机理的温度灵敏度分别为17.29 pm/℃和7.70 pm/℃。

关键词:空芯光纤;级联型光纤器件;反谐振干涉;多模干涉;温度传感
中图分类号:TN253　　**文献标识码**:A　　**doi**:10.3788/gzxb20225111.1106001

0　引言

在工业、农业、医疗、食品加工生产等方面,环境温度的测量必不可少。光纤传感器由于制作简单、抗电磁干扰、耐化学腐蚀及易分布式测量等优点,受到学者们的广泛重视。近年来,空芯光纤(Hollow Core Fiber,HCF)由于其特有的中空结构已经成为光纤传感领域的重要研究对象,基于HCF的传感器件已经被广泛应用在温度传感研究中[1-5]。2015年,吉林大学的ZHU Congcong等通过对拉锥的普通空芯光纤两端分别熔接单模光纤(Single Mode Fiber,SMF)实现了紧凑型光纤传感器,该器件基于多模干涉(Multimode Interference,MMI)机理的温度灵敏度为7.6 pm/℃[4]。2021年,上海大学的YU Yang等将石英毛细管与单模光纤熔接制备级联型传感器件,得到基于反谐振干涉(Anti-resonant,AR)的温度灵敏度为10.0 pm/℃[6]。作为空芯光纤的一种,负曲率反谐振空芯光纤(Negative Curvature Hollow Core Fiber,NCHCF)极大地降低了空芯光纤的传输损耗,其多模干涉和反谐振干涉机理都得到了显著的增强,在温度传感领域更有研究潜力,成为了新的研究热点。

NCHCF在传感应用中同样具有广阔的应用前景。2020年,深圳大学的LIU Dejun首次提出了一种基于NCHCF结构的全光纤干涉仪,利用该器件实现了基于多模干涉的温度及应力传感[7],其温度灵敏度为6.13 pm/℃。2021,南洋理工大学的GOEL C等通过对NCHCF中的MMI机理进行增强,实现了一种紧凑的、温度不敏感且多轴机械力的传感器,温度灵敏度为3.30 pm/℃[8]。目前,实验研究证明了基于MMI机理的NCHCF级联型器件温度传感灵敏度较低,所以学者们开始探究基于AR机理的温度传感。2019年,贝勒大学的WEI Chengli等通过数值仿真研究了一种填充温敏液体的NCHCF温度传感器[9],高损耗谐振峰的波长随温度升高而红移,基于反谐振干涉的理论温度灵敏度为1.10 nm/℃。2021年,东北大学的WANG Qiming等对NCHCF包层管选择性镀膜,并在纤芯中填充酒精,通过数值仿真得到该器件温度灵敏度为3.20 nm/℃[10]。2022年,燕山大学的CHEN Qiang仿真设计了基于表面等离子体和反谐振效应的负曲率空芯光纤温度传感器,在光纤的包层管内壁镀金属薄膜,并在纤芯中填充温敏液体,数值计算的温度灵敏度为1.07 nm/℃[11]。目前的研究结果表明,大多基于AR机理的温度传感研究以数值仿真为主。通过在纤芯中填

基金项目:国家自然科学基金(Nos. 62022053, 61875116),111计划(No. D20031),上海市科委项目(Nos. 22010500100, 22ZR1424800)
第一作者:汪柯红(1997—),女,硕士研究生,主要研究方向为光纤传感器研究。Email:peachred@shu.edu.cn
导师(通讯作者):张小贝(1982—),男,教授,博士,主要研究方向为特种光纤器件、光学谐振腔和光纤传感研究。Email:xbzhang@shu.edu.cn
收稿日期:2022-03-14;**录用日期**:2022-05-13

充温敏液体从而使得基于AR机理的温度传感灵敏度高，这对器件的制备带来了一定的挑战。为了简化器件的制备并获得高温度传感灵敏度，本文从解析公式上理论证明了无填充液体时，基于AR机理的温度传感灵敏度仍然高于MMI，且进行了实验证明。

本文采用单模光纤、渐变折射率多模光纤（Graded-Index Fiber，GIF）和负曲率反谐振空芯光纤熔接制备成五段式级联型光纤传感器件，基于反谐振干涉和MMI双机理实现温度传感。首先仿真分析了空芯光纤的模场分布及传输特性，并基于光纤材料的热光和热膨胀效应，理论分析了温度传感器件的工作原理。通过合适的熔接参数成功制备该级联型传感器件，并对其温度传感特性进行了双机理比较研究。

1 器件制备

本文研究的负曲率反谐振空芯光纤横截面结构如图1(a)所示，其中纤芯内径D为45 μm，包层管内径d为30 μm，包层管壁厚t为1.2 μm；空气纤芯的折射率为1，包层材料为石英，根据二氧化硅折射率的塞米尔方程[12]，包层材料在1 550 nm处折射率为1.448。

通过普通电弧熔接机（FITEL-S179）、二氧化碳激光熔接机（Fujikura-LZM-100）的熔接平台以及精密切割平台，加工制备了SMF-GIF-NCHCF-GIF-SMF级联型温度传感器件。所使用的光纤包括单模光纤（美国康宁公司SMF-28）、渐变折射率多模光纤（长飞公司OM1）和暨南大学研制的负曲率反谐振空芯光纤。其中，空芯光纤去掉涂覆层后外径为240 μm，选用高精度大芯径切割刀（Fujikura-CT-104）对空芯光纤进行切割，得到平整的截面如图1(a)所示。为了提高单模光纤与空芯光纤之间的耦合效率，采用多模光纤作为过渡光纤，能减少因光纤模场失配造成的耦合损耗；渐变折射率多模光纤相较阶跃折射率多模光纤，激发的模式较少。当光通过SMF入射到GIF时，光场在GIF长度为550 μm处时发散到最大，且GIF的自聚焦位置间隔是等距的[13]，图1(b)为五段式级联型器件的结构示意图，在本器件中选用GIF的长度为5.3 cm，NCHCF的长度为3.1 cm。

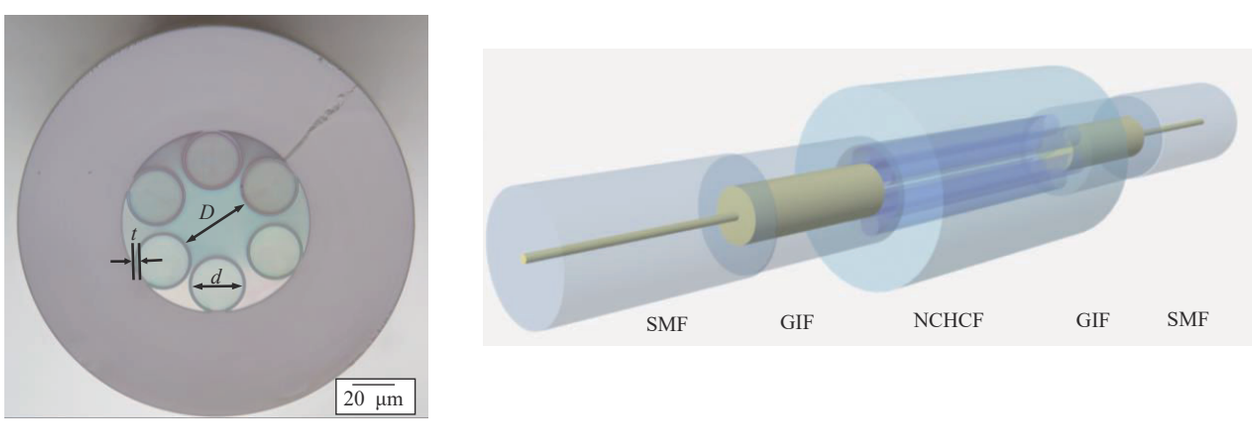

(a) Cross section of NCHCF　　(b) Schematic diagram of the cascaded structure

图1 SMF-GIF-NCHCF-GIF-SMF级联型温度传感器结构示意图

Fig.1 Schematic diagram of the SMF-GIF-NCHCF-GIF-SMF temperature sensor

2 温度传感原理

本文主要对基于AR和MMI两种传输机理的温度传感特性进行比较，其传输光路分别如图2所示。对于AR模型，在光传输的过程中，其空芯/包层界面反射回纤芯的光与包层/外部空气界面反射回纤芯的光会发生干涉，如图2(a)所示，在谐振波段，返回纤芯的光束发生相消干涉，则光会被限制在高折射率的包层中传输，从而造成高损耗；而在反谐振波段，返回纤芯的光束发生相长干涉。在NCHCF中大部分光会被限制在纤芯中传输，且多个纤芯模式被激发从而产生MMI，如图2(b)所示。

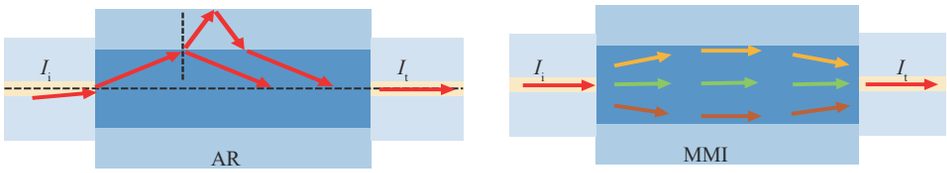

(a) The optical path diagrams of the AR　　(b) The optical path diagrams of the MMI

图2　基于NCHCF的级联型结构的AR和MMI传感机理的光路图

Fig.2　The optical path diagrams of the AR and MMI transmission mechanisms in NCHCF cascaded structure

2.1　多模干涉机理

采用COMSOL软件有限元分析法对NCHCF的模式进行数值求解[15]。在不考虑偏芯激发且在高斯光场的激励下，由于光纤结构的对称性，光纤中只有本征模式LP_{0n}会被激发[16]。经数值计算得到纤芯基模、高阶模式及包层管基模的模场分布如图3所示。包层模式主要包括在高折射率区域的介电模式和空气区域的泄漏模式（管模）两种[17]。NCHCF的纤芯模式主要集中在空气纤芯中，由于纤芯内径较大，可容纳多种模式，且各个模式的传播常数不同，在传输过程中会发生多模干涉效应，其干涉峰波长的计算公式为$\lambda_m = L\left(n_p - n_q\right)/m$。其中，$L$为传播长度，$n_p$和$n_q$分别对应两干涉模式的有效折射率，$m$为阶次[8]。

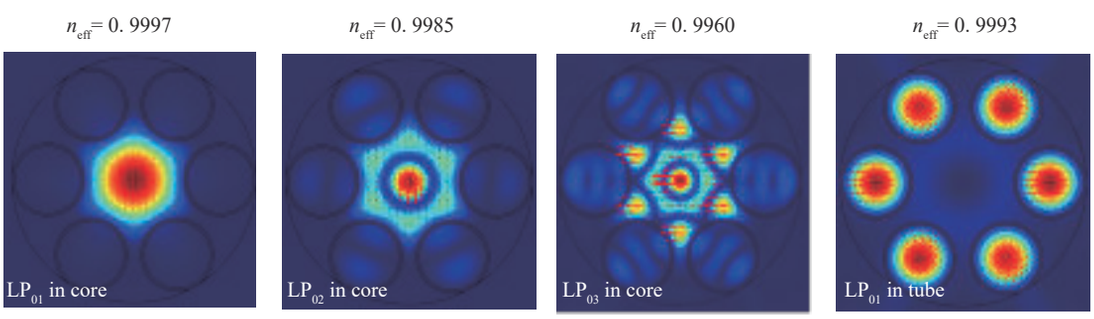

图3　负曲率反谐振空芯光纤的模式分布

Fig.3　Mode field distribution of NCHCF

级联型传感器件基于光纤的热光效应和热膨胀效应实现温度传感。根据热光效应，温度的变化会引起包层及空气纤芯折射率的改变，从而对空芯光纤中支持模式的有效折射率造成影响，同时光纤的长度会因材料的热膨胀效应发生改变，模间干涉产生的干涉峰位置会发生偏移。因此可通过监测基于MMI传输机理的干涉峰位置的变化来表征外界温度的变化，多模干涉效应的干涉峰波长的计算公式为$\lambda_m = L\left(n_p - n_q\right)/m$，当温度上升时，光纤长度$L$会增加，干涉峰发生红移。将MMI干涉峰波长对温度求偏导，得到其温度灵敏度的计算表示为[6]

$$S_{T,\mathrm{MMI}} = \frac{\Delta\lambda}{\Delta T} = \left(\frac{\Delta n_p}{\Delta T} - \frac{\Delta n_q}{\Delta T}\right)\frac{L}{m} + \frac{\Delta L}{\Delta T}\left(\frac{n_p - n_q}{m}\right) = \left(\frac{1}{n_p}\frac{\Delta n_p}{\Delta T}n_p - \frac{1}{n_q}\frac{\Delta n_q}{\Delta T}n_q\right)\frac{L}{m} + \frac{1}{L}\frac{\Delta L}{\Delta T}L\left(\frac{n_p - n_q}{m}\right) \quad (1)$$

式中，$S_{T,\mathrm{MMI}}$是多模干涉机理对应的温度灵敏度，可以表示为单位温度下波长的偏移量大小$\Delta\lambda/\Delta T$，Δn_p和Δn_q为发生干涉的两个模式的有效折射率的变化值。

2.2　反谐振干涉机理

对于空芯光纤，其导光机理可用反谐振干涉进行解释[18]。将其包层管壁等效为高折的法布里-珀罗腔，谐振波长的计算公式为$\lambda_m = (2t/m)\sqrt{n_2^2 - n_1^2}$[19]。其中，$\lambda_m$为谐振波长，$t$为包层管壁厚，$n_1$和$n_2$分别为纤芯和包层的有效折射率，谐振阶数$m$为1至4时对应的谐振波长分别为2 513.37 nm，1 256.68 nm，837.79 nm和628.34 nm。根据限制损耗公式$\mathrm{Loss} = 8.686(2\pi/\lambda)\mathrm{Im}\left(n_{eff}\right)$，仿真计算的纤芯基模的损耗谱如图4所示，其中$\mathrm{Im}(n_{eff})$是模式有效折射率的虚部[20]。当传输波长满足谐振条件时，光束发生相消干涉，如点A对应的模场分布所示，此时传输损耗较高；当传输波长满足反谐振条件时，光束发生相长干涉，光场主要被限制在纤

芯中，如点B对应的模场分布。空芯光纤凭借其负曲率结构及较小的包层管壁厚，在包层的高折射率材料中支持的介电模式与纤芯基模的场重叠积分面积较小，从而包层模式与纤芯基模之间的耦合被抑制，因此，在反谐振条件下可以实现低损耗传输。其反谐振干涉得到增强，谐振峰的消光比更大，更有利于传感应用。

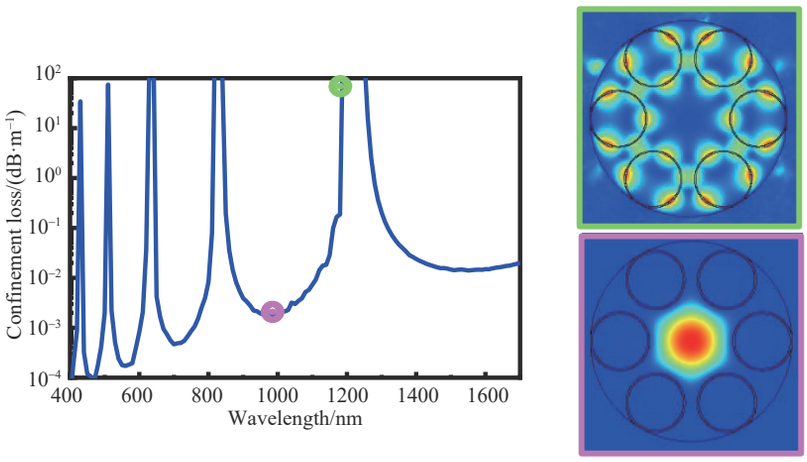

图4 负曲率反谐振空芯光纤的纤芯基模的损耗仿真

Fig. 4 The simulation results for the loss of core fundamental mode in NCHCF with different wavelengths

根据材料的热膨胀和热光效应，温度的变化也会影响包层管壁厚及光纤材料，从而基于AR机理的谐振波长会发生偏移。谐振波长为$\lambda_m=(2t/m)\sqrt{n_2^2-n_1^2}$，温度上升时，包层的折射率$n_2$和壁厚$t$均会增加，而空气的折射率$n_1$减小，谐振峰会随温度的升高而往长波长方向移动。将谐振波长对温度求偏导，得到基于AR机理的温度传感灵敏度可以表示为[6]

$$\begin{aligned}S_{T,\mathrm{AR}}&=\frac{\Delta\lambda}{\Delta T}=\frac{2}{m}\left[\frac{\Delta t}{\Delta T}\sqrt{{n_2}^2-{n_1}^2}+\frac{\Delta n_2}{\Delta T}\frac{tn_2}{\sqrt{{n_2}^2-{n_1}^2}}-\frac{\Delta n_1}{\Delta T}\frac{tn_1}{\sqrt{{n_2}^2-{n_1}^2}}\right]\\&=\frac{2}{m}\left[(1/t)\frac{\Delta t}{\Delta T}t\sqrt{{n_2}^2-{n_1}^2}+(1/n_2)\frac{\Delta n_2}{\Delta T}\frac{{tn_2}^2}{\sqrt{{n_2}^2-{n_1}^2}}-(1/n_1)\frac{\Delta n_1}{\Delta T}\frac{{tn_1}^2}{\sqrt{{n_2}^2-{n_1}^2}}\right]\end{aligned}\tag{2}$$

式中，$S_{T,\mathrm{AR}}$是反谐振干涉对应的温度灵敏度，$(1/t)\Delta t/\Delta T$是材料的热膨胀系数，表示单位温度下包层管壁厚的变化情况。NCHCF的包层材料为石英材料，热膨胀系数为0.55×10^{-6} /℃。$(1/n)\Delta n/\Delta T$表示单位温度变化下不同材料折射率的变化，石英材料和空气的热光系数分别为6.45×10^{-6} /℃和-0.93×10^{-6} /℃[34]。将光纤材料参数代入式(2)可求得基于AR机理的温度传感灵敏度为17.25 pm/℃。其中，由光纤包层材料的热光效应引起的温度灵敏度为15.5 pm/℃。

光纤包层材料的热光效应对温度传感起主导作用，因此，仅考虑包层材料的热光效应，对不同温度下二阶谐振波长处纤芯基模的限制损耗进行仿真，仿真结果如图5所示。λ_1和λ_2的波长漂移如图5(a)内嵌所示，随着温度的增加，曲线均呈红移现象[9]。对峰值进行线性拟合，得到拟合结果如图5(b)所示，温度传感灵敏度为15.57 pm/℃，与理论计算结果一致。

基于AR的温度传感灵敏度与包层材料的热光效应相关，而基于MMI的温度传感灵敏度仅与空气纤芯的热光效应相关，由于NCHCF包层材料的热光系数比空气更大，因此AR机理对温度的变化更为敏感。此外，通过空芯光纤的模式计算模型可知，该模型只针对传播常数近似等于自由空间的传播常数的低损耗模式，相较于MMI机理发生干涉的两个模式间的有效折射率差值$(n_\mathrm{p}-n_\mathrm{q})$约为$10^{-3}$量级，AR机理中包层和空气纤芯的有效折射率差$(n_2-n_1)$为0.448。因此，对比式(1)和(2)可得到结论：基于AR的理论温度传感灵敏度高于MMI。

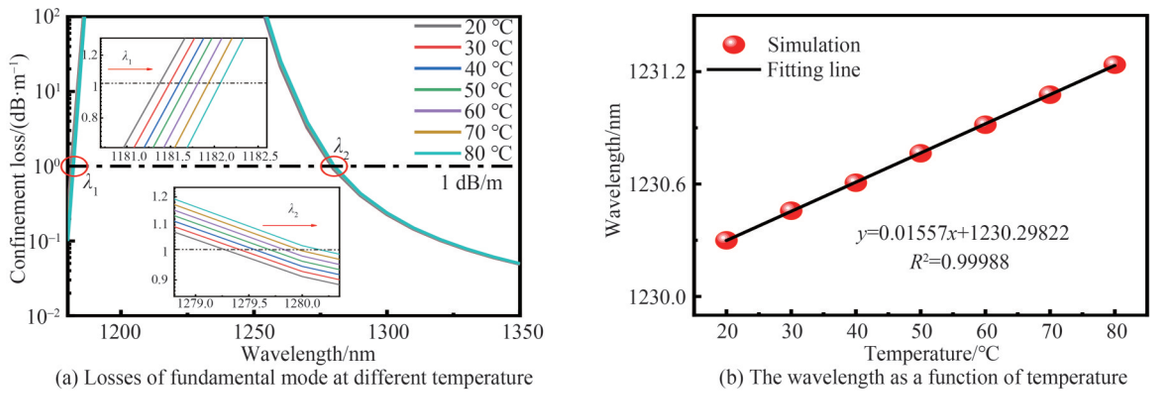

(a) Losses of fundamental mode at different temperature　(b) The wavelength as a function of temperature

图5　不同温度下负曲率反谐振空芯光纤的纤芯基模的损耗仿真

Fig.5　The simulation results for the losses of core fundamental mode in NCHCF at different temperature

3　传感实验与讨论

3.1　传感实验系统

实验系统如图6所示，温度传感器两端分别连接宽带光源（Broadband Source，BBS）和光谱分析仪（Optical Spectrum Analyzer，OSA）。由于NCHCF的相邻AR谐振峰之间的传输带宽较大，因此将光谱仪的监测波长设置为600～1 700 nm，且光谱仪的分辨率设置为0.02 nm。将级联型传感器件放置在温控箱（ESL-04 ESEPC），通过程序调节箱内的温度，设定温控箱以10 ℃为步长，温度测量范围为20～80 ℃。每次改变温度，均在温度稳定后再记录数据。为了增加温度测量的精确度，将热电偶放置于传感器的附近来实时监测传感器周围的温度。

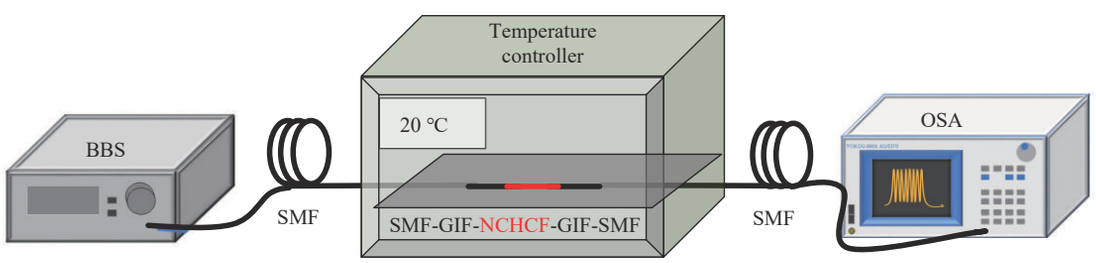

图6　温度传感实验装置图

Fig. 6　Schematic diagram of temperature sensing experimental setup

3.2　传感实验结果与讨论

基于NCHCF的级联型器件在不同温度下的透射谱如图7所示。从透射谱中可以观察到两个明显的谐振波长区域，分别对应于AR的二阶和三阶谐振波长。每个谐振区域存在三个谐振峰，分别对应于NCHCF支持的LP_{01}，LP_{02}和LP_{03}三个AR模式。在相邻的谐振波长区域之间存在低损传输带，由于纤芯内模式之间发生多模干涉，该范围内谱线存在周期性振荡。

考虑到谐振峰的损耗，对MMI的干涉峰以及AR的谐振峰dip 1分别进行监测，波长漂移情况分别如图8(a)和图8(b)所示。随着温度的升高，透射谱的形状基本保持不变。在热膨胀和热光效应的共同作用下，包层的折射率以及壁厚均会随着温度的升高而增大，而空气的折射率会减小。因此，MMI的干涉峰以及AR的谐振峰均呈红移现象，与式(1)和公式(2)的理论分析结果一致。

进行多次实验并得到四组不同温度下MMI干涉峰和AR谐振峰的变化规律，对每一温度测量得到的峰值数据进行带误差拟合，结果如图9所示。在温度测量范围内，监测1 500 nm波长处的MMI干涉峰，波长会随着温度的升高呈线性变化趋势，拟合得到其温度传感灵敏度为7.70 pm/℃，线性度为96.56%。精度（检测极限）DL由器件灵敏度S和仪器分辨率R决定，定义为$DL=R/S$[21]，光谱仪的分辨率R为0.02 nm，由此计

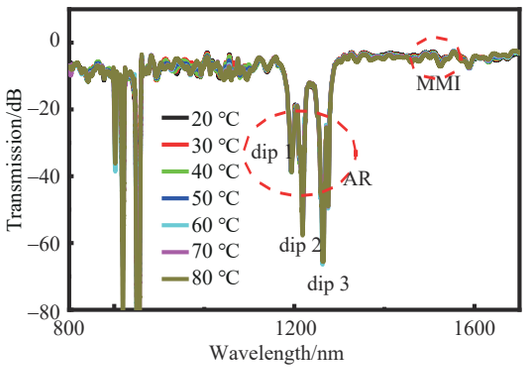

图 7 SMF-GIF-NCHCF-GIF-SMF 温度传感器件的透射谱

Fig. 7 Transmission spectra of the SMF-GIF-NCHCF-GIF-SMF for temperature sensing

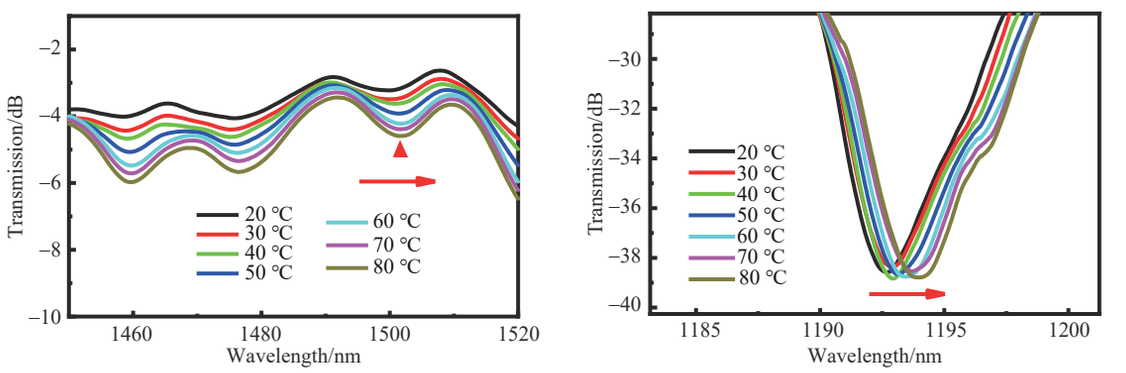

(a) Transmission spectra of MMI with different temperatures

(b) Transmission spectra of AR with different temperatures

图 8 负曲率反谐振空芯光纤基于 AR 和 MMI 的温度传感实验测试结果

Fig.8 The experimental results of NCHCF temperature sensing based on AR and MMI

算得到该机理的精度是 2.60 ℃。由于器件的结构以及发生干涉的模式有效折射率存在差异，本文得到的基于 MMI 五段式 NCHCF 传感器件的温度传感结果比目前已有的三段式结构的灵敏度 6.13 pm/℃[7]略高。监测 AR 谐振峰 dip 1，温度与波长呈线性关系，温度传感灵敏度为 17.29 pm/℃，线性度为 99.58%，与式(2)计算的理论灵敏度 17.25 pm/℃基本一致，计算得到基于 AR 机理的精度为 1.16 ℃。此外，通过线性拟合 AR 谐振峰 dip 2 和 dip 3，得到其温度传感灵敏度分别为 17.38 pm/℃和 17.22 pm/℃。三个 AR 谐振峰的温度传感灵敏度基本一致，并与理论分析结果一致。对比上述实验结果可知基于 AR 机理的温度传感灵敏度更高，并且可以实现更加精细的温度检测。

比较级联型传感器在不同传输机理下的温度传感实验结果，器件的透射谱会随着温度的升高发生红移。温度变化时，不同机理的响应灵敏度不同，AR 机理的温度传感灵敏度明显优于 MMI，与之前的理论分析一致。由此说明对基于负曲率反谐振空芯光纤的级联型传感器而言，反谐振干涉机理在温度传感的应用场景下更占优势。器件的温度测量范围主要与其石英包层材料特性相关，本文主要在 20～80 ℃温度范围进行了器件的温度传感实验，而现已有相关研究表明基于石英材料器件的检测温度能高达 1 100 ℃[22]因此，该传感器件可以在更高的温度环境下应用。

4 结论

本文研制了基于负曲率反谐振空芯光纤的级联型光纤温度传感器。仿真分析了空芯光纤纤芯模式和包层模式的模场分布。在此基础上，理论分析了基于 AR 和 MMI 传输机理的温度传感原理。由于光纤材料的热膨胀和热光效应，器件基于 AR 机理的温度传感灵敏度相较于 MMI 更高。实验结果表明基于 AR 机理的温度传感灵敏度可达 17.29 pm/℃，而基于 MMI 的温度灵敏度仅有 7.70 pm/℃，因此 AR 机理更适合该器件的温度传感应用，同时本文提出的传感器件具有稳定性好和灵敏度高等优点，可广泛应用于环境温度检

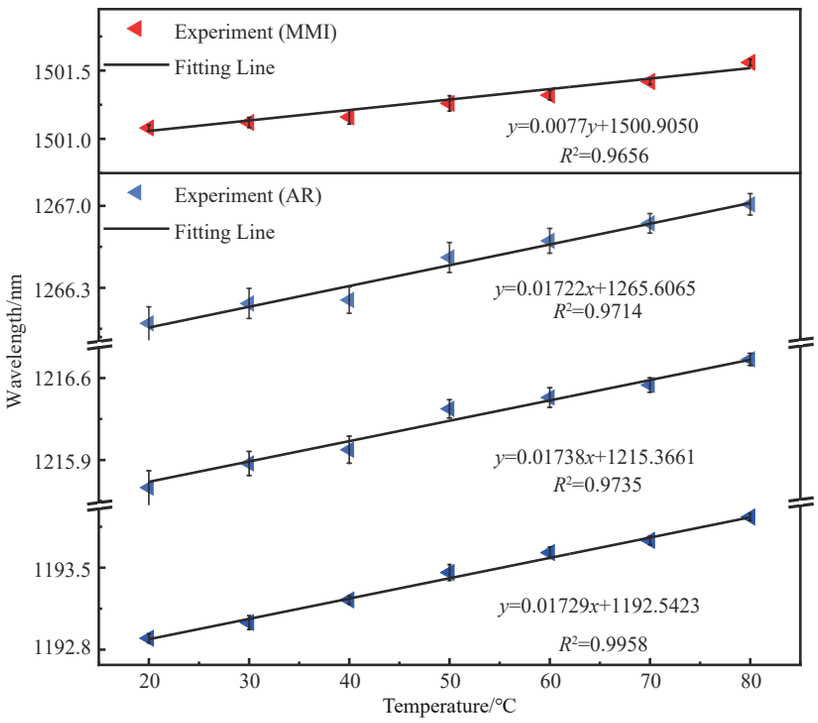

图9　基于MMI和AR的谐振波长与温度的关系

Fig.9　The relationship between wavelength and temperature based on MMI and AR

测场景。

参考文献

[1] SHEN Jiaxin, WANG Wei, ZHANG Junying, et al. Hybrid temperature and strain dual-parameter sensor based on fiber Bragg grating and multi-mode interference of hollow-core fiber[J]. Acta Photonica Sinica, 2021, 50(5): 0506006.
申佳鑫，王伟，张军英，等. 光纤布拉格光栅与空芯光纤多模干涉混合型温度应变双参量传感器[J]. 光子学报，2021，50(5)：0506006.

[2] HOU Leyi, MAO Bangning, WANG Jianfeng, et al. Temperature characteristics of cascaded Fabry-Perot interferometer sensors based on vernier effect[J]. Acta Photonica Sinica, 2019, 48(9): 0906002.
侯乐义，毛邦宁，王剑锋，等. 基于游标效应的级联法布里-珀罗传感器温度特性[J]. 光子学报，2019，48(9)：0906002

[3] LIU Tianmu, JIANG Yi, CUI Yang, et al. Photonic crystal fiber temperature and pressure sensor[J]. Acta Photonica Sinica, 2020, 49(4): 0406001.
刘天沐，江毅，崔洋. 光子晶体光纤温度压力传感器[J]. 光子学报，2020，49(4)：0406001.

[4] ZHU C, YU Y, ZHANG Y, et al. Compact Mach-Zehnder interferometer based on tapered hollow optical fiber[J]. Photonics Technology Letters, 2015, 27(12):1277-1280.

[5] YU H, LUO Z, ZHENG Y, et al. Temperature-insensitive vibration sensor with Kagomé hollow-core fiber based Fabry-Perot interferometer[J]. Journal of Lightwave Technology, 2019, 37(10):2261-2269.

[6] YU Y, ZHANG X, WANG K, et al. Coexistence of transmission mechanisms for independent multi-parameter sensing in a silica capillary-based cascaded structure [J]. Optics Express, 2021, 29(17): 27938-279350.

[7] LIU D, LI W, WU Q, et al. Negative curvature hollow core fiber based all-fiber interferometer and its sensing applications to temperature and strain [J]. Sensors, 2020, 20(17): 1-12.

[8] GOEL C, ZANG J, PARROT M, et al. Temperature-insensitive mechanical sensor using multi-modal behavior of antiresonant hollow-core fibers [J]. Journal of Lightwave Technology, 2021, 39(12): 3998-4005.

[9] WEI C, YOUNG J T, MENYUK C R, et al. Temperature sensor based on liquid-filled negative curvature optical fibers [J]. OSA Continuum, 2019, 2(7): 2123-2130.

[10] WANG Q, ZHANG X, YAN X, et al. Design of a surface plasmon resonance temperature sensor with multi-wavebands based on conjoined-tubular anti-resonance fiber[J]. Photonics, 2021, 8(6):231-231.

[11] CHEN Q, CHEN H, LIU Y D, et al. A self-verification temperature sensor based on surface plasmon resonance in a hollow core negative curvature fiber[J]. Journal of Physics D: Applied Physics, 2022, 55(22): 225208-225208.

[12] WANG J, PEI L, WANG J, et al. Design and analysis for large-mode-area photonic crystal fiber with negative-curvature

air ring [J]. Optical Fiber Technology, 2021, 62(11):102478-102478.
[13] HOFMANN P, MAFI A, JOLLIVET C, et al. Detailed investigation of mode-field adapters utilizing multimode-interference in graded index fibers [J]. Journal of Lightwave Technology, 2012, 30(14): 2289-2298.
[14] SUN W, ZHANG X, YU Y, et al. Comparative study on transmission mechanisms in a SMF-capillary-SMF structure [J]. Journal of Lightwave Technology, 2020, 38(1): 1-11.
[15] MARCATILI E A J, SCHMELTZER R A. Hollow metallic and dielectric waveguides for long distance optical transmission and lasers [J]. The Bell System Technical Journal, 1964, 43(4): 1783-1809.
[16] HOFMANN P, MAFI A, JOLLIVET C, et al. Detailed investigation of mode-field adapters utilizing multimode-interference in graded index fibers [J]. Journal of Lightwave Technology, 2012, 30(14): 2289-2298.
[17] VINCETTI L, SETTI V. Waveguiding mechanism in tube lattice fibers [J]. Optics Express, 2010, 18(22): 23133-23146.
[18] DING Wei, WANG Yingying, GAO Shoufei, et al. Theoretical and experimental investigation of light guidance in hollow-core anti-resonant fiber [J]. Acta Physica Sinica, 2018, 67(12):124201-124201.
丁伟, 汪滢莹, 高寿飞, 等. 高性能反谐振空芯光纤导光机理与实验制作研究进展[J]. 物理学报, 2018, 67(12): 124201-124201.
[19] LITCHINITSER N M, ABEELUCK A K, HEADLEY C, et al. Antiresonant reflecting photonic crystal optical waveguides [J]. Optics Letters, 2002, 27(18): 1592-1594.
[20] YU F, SONG P, WU D. Attenuation limit of silica-based hollow-core fiber at mid-IR wavelengths [J]. APL Photonics, 2019, 4(8): 1-6.
[21] CHAO Y, GUO J. Design and optimization of microring resonators in biochemical sensing applications [J]. Journal of Lightwave Technology, 2006, 24(3):1395-1402.
[22] ZHANG Z, XU B, ZHOU M, et al. Hollow-core fiber-tip interferometric high-temperature sensor operating at 1100 ℃ with high linearity[J]. Micromachines, 2021, 12(3): 234.

Comparative Study on Temperature Sensing Characteristics of Dual Mechanisms in Hollow Core Fiber

WANG Kehong, YU Yang, WANG Yang, LIU Xiaochen, ZHAO Shuaichang, YANG Yong, ZHANG Qi, ZHANG Xiaobei

(*Key Laboratory of Specialty Fiber Optics and Optical Access Networks, School of Communication and Information Engineering, Shanghai University, Shanghai* 200444, *China*)

Abstract: The ambient temperature sensing is essential in industry, agriculture, medicine, food processing and so on. Optical fiber sensors have been widely valued by scholars due to the advantages of simple fabrication, electromagnetic interference resistance, chemical corrosion resistance and easily distributed measurement. In recent years, Hollow Core Fiber (HCF) has been investigated in fiber temperature sensing due to its hollow structure. In addition, antiresonant Negative Curvature Hollow Core Fiber (NCHCF) as a special hollow photonic crystal fiber, greatly reduces transmission loss of HCF by virtue of its negative curvature structure and quite thin cladding tube wall thickness. Hence, the mechanism of Multimode Interference (MMI) and Anti-Resonant (AR) of NCHCF are significantly enhanced, so it has more potential in the field of sensing and has become the focus in optical fiber sensing. At present, the sensitivity of the NCHCF cascaded temperature sensor based on the MMI mechanism is low. And some simulations have indicated that the high temperature sensitivity based on AR mechanism can be obtained by filling temperature-sensitive liquid into the hollow core of NCHCF. In order to simplify the fabrication of devices and obtain high temperature sensing sensitivity, the temperature sensing characteristics of the unfilled cascaded device based on AR and MMI are both studied theoretically and experimentally in this paper. Firstly, Single-Mode Fiber (SMF), Graded Index Fiber (GIF) and NCHCF are fused to form the cascaded fiber sensing structure (SMF-GIF-NCHCF-GIF-SMF). And then, the temperature sensing principle of the cascaded sensor based on MMI and AR is analyzed and the formulas are deduced. As temperature increases, the tube wall thickness and the refractive index of cladding and will increase due to the thermal expansion and thermal-optical effect of fiber materials, while the refractive index of air will

decrease. Therefore, the dips based on MMI and AR both show red shift with the increases of temperature. The temperature sensitivity based on AR resonant dip is calculated as 17.25 pm /℃, and the sensitivity only caused by the thermo-optic effect of the fiber cladding material is 15.50 pm/℃. It is concluded that the thermo-optic effect of the fiber cladding material should play a leading role in temperature sensing. Therefore, the confinement losses of the core fundamental mode at corresponding resonant wavelength vary with different temperatures are simulated, where only the thermo-optic effect of the fiber cladding material is considered. And the simulation result is 15.57 pm/℃, which is consistent with the theoretical calculation. Finally, the temperature sensing experimental setup is designed and built. The temperature sensor is placed in the temperature controller and the endpoints of the sensor are connected with Broadband Light Source (BBS) and Optical Spectrum Analyzer (OSA), respectively. As the transmission bandwidth between adjacent AR resonant dips of NCHCF is large, the range of monitoring wavelength of the OSA is set as 600～1 700 nm, and its resolution is 0.02 nm. Multiple experiments are performed for monitoring MMI and AR dips when the temperature increases from 20 to 80 ℃ at a step of 10 ℃. It is found that the wavelength of each dip shifts as a function of temperature, which is fitted with an error bar. And the experimental results show that the temperature sensitivity and Detection Limit (DL) based on the MMI mechanism are 7.70 pm/℃ and 2.60 ℃, respectively. As for AR based sensors, there are three resonant dips in the resonant region of the transmission spectrum, which correspond to the three AR modes supported by NCHCF. The temperature sensitivities of the three dips are 17.29 pm/℃, 17.38 pm/℃ and 17.22 pm/℃, respectively, which are consistent with the theoretical results. And the DL based on AR mechanism is 1.16 ℃. Compared with the above experimental results, the temperature sensor based on AR mechanism has higher sensitivity and more fine detection, and thus AR mechanism is more suitable for temperature sensing. The temperature sensing experiment of the cascaded device is mainly carried out in the temperature range of 20～80 ℃. However, the relevant studies have shown that the detection temperature based on the quartz material sensor can be up to 1 100℃. Therefore, the proposed sensor can be used in a higher temperature environment theoretically. Meanwhile, it has the advantage of good stability and can be widely used in environmental temperature detection scenes. In addition, the comparative study of dual mechanisms carried out in this paper can provide the theoretical basis for multi-parameter sensing.

Key words: Hollow core fiber; Cascaded fiber device; Anti-resonant; Multimode interference; Temperature sensor

OCIS Codes: 060.2270; 060.2310; 060.2370; 060.2400

Foundation item: National Natural Science Foundation of China (Nos. 62022053, 61875116), 111 Project (No. D20031), Science and Technology Commission of Shanghai Municipality (Nos. 22010500100, 22ZR1424800)